大 气 科 学 1998
*Chinese Journal of Atmospheric Sciences*
Volume 22, No.4, pp. 481–503

# A Three–Dimensional Numerical Simulation of the South China Sea Circulation and Thermohaline Structure

*Peter C. Chu*(朱伯承) and *Nathan L. Edmons*
(Department of Oceanography, Naval Postgraduate School, Monterey, CA 93943, U.S.A.)

Manuscript recieved June 25, 1998; revised October 14, 1998.

The seasonal ocean circulation and thermal structure in the South China Sea (SCS) were studied numerically using the Princeton Ocean Model (POM) with 20 km horizontal resolution and 23 sigma levels conforming to a realistic bottom topography. A sixteen month control run was performed using climatological monthly mean wind stresses, restoring type surface salt and heat, and observational oceanic inflow / outflow at the open boundaries. The seasonally averaged effects of isolated forcing terms are presented and analyzed from the following experiments: 1) non–linear dynamic effects removed, 2) wind effects removed, 3) open boundary inflow / outflow set to zero. This procedure allowed analysis of the contribution of individual parameters to the general hydrology and specific features of the SCS, for example, coastal jets, mesoscale topographic gyres, and counter currents. Our results show that the POM model has capability of simulating seasonal variations of the SCS circulation and thermohaline structure. The simulated SCS surface circulation is generally anticyclonic (cyclonic) during summer (winter) monsoon period with a strong western boundary current, with a mean maximum speed of 0.5 m / s (0.95 m / s), mean volume transport of 5.5 Sv (10.6 Sv), extending to a depth of around 200 m (500 m). During summer, the western boundary current splits and partially leaves the coast; the bifurcation point is at 14°N in May, and shifts south to 10°N in July. Besides, a mesoscale eddy in the Sunda Shelf (Natuna Island Eddy) was also simulated. This eddy is anticyclonic (cyclonic) during summer (winter) monsoon with maximum swirl velocity of 0.6 m / s at the peak of the winter monsoon. The simulated thermohaline structure for summer and winter is nearly horizontal from east to west except at the coastal regions. Coastal upwelling and downwelling are also simulated: localized lifting (descending) of the isotherms and isohalines during summer (winter) at the west boundary. The simulation is reasonable comparing to the observations. Sensitivity experiments were designed to investigate the driving mechanisms. Non–linearity is shown to be important to the transport of baroclinic eddy features, but otherwise insignificant. Transport from lateral boundaries is of considerable importance to summer circulation and thermal structure, with lesser effect on winter monsoon hydrology. In general, seasonal circulation patterns and upwelling phenomena are determined and forced by the wind, while the lateral boundary forcing plays a secondary role in determining the magnitude of the circulation velocities.

**Key words**: numerical simulation; circulation; South China Sea.

## 1. INTRODUCTION

The South China Sea (SCS) is a semi–enclosed tropical sea located between the Asian land mass to the north and west, the Philippine Islands to the east, Borneo to the southeast,

and Indonesia to the south (Fig. 1), a total area of $3.5 \times 10^6$ km$^2$. It includes the shallow Gulf of Thailand and connections to the East China Sea (through the Taiwan Strait), the Pacific Ocean (through the Luzon Strait), the Sulu Sea (through the Mindoro Strait), the Java Sea (through the Gasper and Karimata Straits) and to the Indian Ocean (through the Strait of Malacca). All of these straits are shallow except the Luzon Strait whose maximum depth is 1800 m. Consequently the SCS is considered a semi-enclosed water body[1]. The complex topography includes the broad shallows of the Sunda Shelf in the south / southwest; the continental shelf of the Asian landmass in the north, extending from the Gulf of Tonkin to the Taiwan Strait; a deep, elliptical shaped basin in the center, and numerous reef islands and underwater plateaus scattered throughout. The shelf that extends from the Gulf of Tonkin to the Taiwan Strait is consistently near 70 m deep, and averages 150 km in width; the central

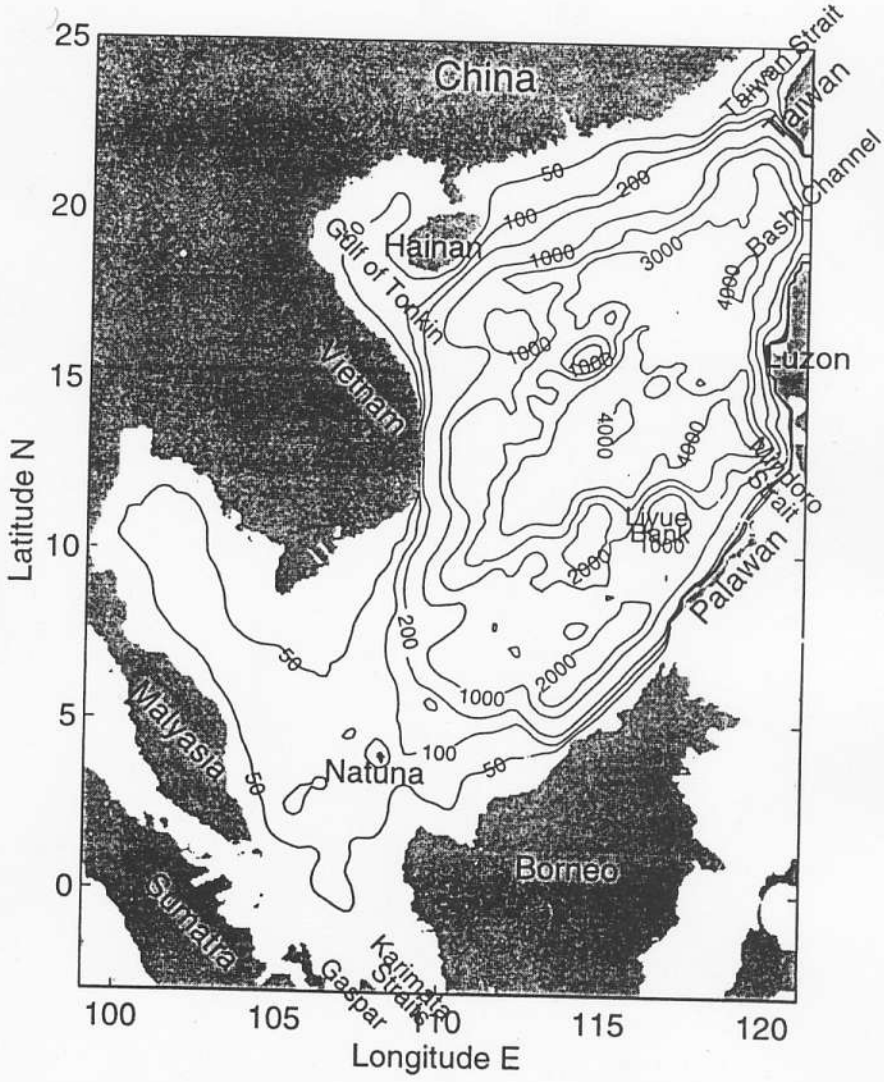


FIGURE 1. Geography and isobaths showing the bathymetry (m) of the South China Sea.

deep basin is 1900 km along its major axis (northeast–southwest) and approximately 1100 km along its minor axis, and extends to over 4000 m deep. The Sunda Shelf is the submerged connection between southeast Asia, Malaysia, Sumatra, Java, and Borneo and is 100 m deep in the middle; the center of the Gulf of Thailand is about 70 m deep.

The SCS is subjected to a seasonal monsoon system[2]. From April to August, the weaker southwesterly summer monsoon winds result in a wind stress of over 0.1 N / $m^2$ (Fig. 2a) which drives a northward coastal jet off Vietnam and anticyclonic circulation in the SCS (Fig. 3a). From November to March, the stronger northeasterly winter monsoon winds corresponds to a maximum wind stress of nearly 0.3 N / $m^2$ (Fig. 2b) causing a southward coastal jet and cyclonic circulation in the SCS (Fig. 3b). The transitional periods are marked by highly variable winds and surface currents.

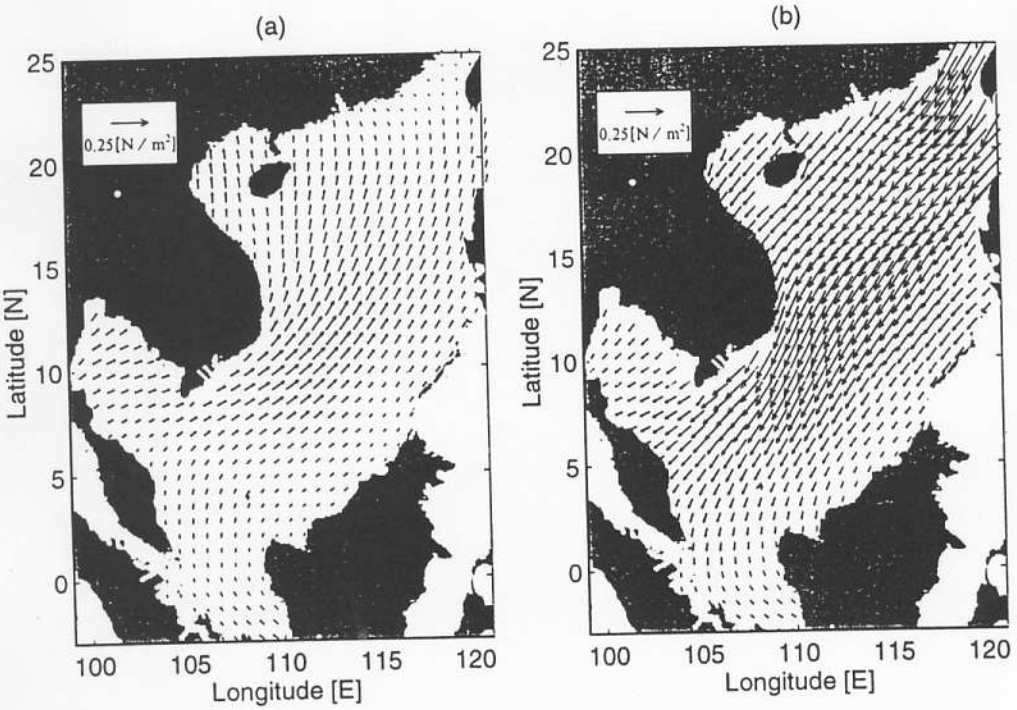


FIGURE 2. Climatological wind stress (0.1 N / $m^2$) for (a) June, and (b) December (after Ref. [3]).

The observed circulation patterns of the intermediate to upper layers of the SCS are primarily forced by the local monsoon systems[2], with contributions from the Kuroshio Current via the Bashi Channel, in the southern half of the Bashi Channel. The Kuroshio enters the SCS through the southern side of the channel then executes a tight, anticyclonic turn and exits the SCS near Taiwan. An estimated 8–10 Sv (1 Sv = $10^6$ $m^3$ / s) of the intrusion passes through the Bashi Channel[1]. This flow exerts a strong influence on the properties of the northern SCS waters and is believed to contribute to currents in the Taiwan Strait[4].

Eddy behavior in the SCS has two distinct features. First, the number of cold eddies is far greater than the number of warm eddies and second, the eddies are significantly affected by the bottom topography and are most likely to occur near localized high current velocity[1]. Small scale eddies with seasonal dependence have been found off coastal Vietnam

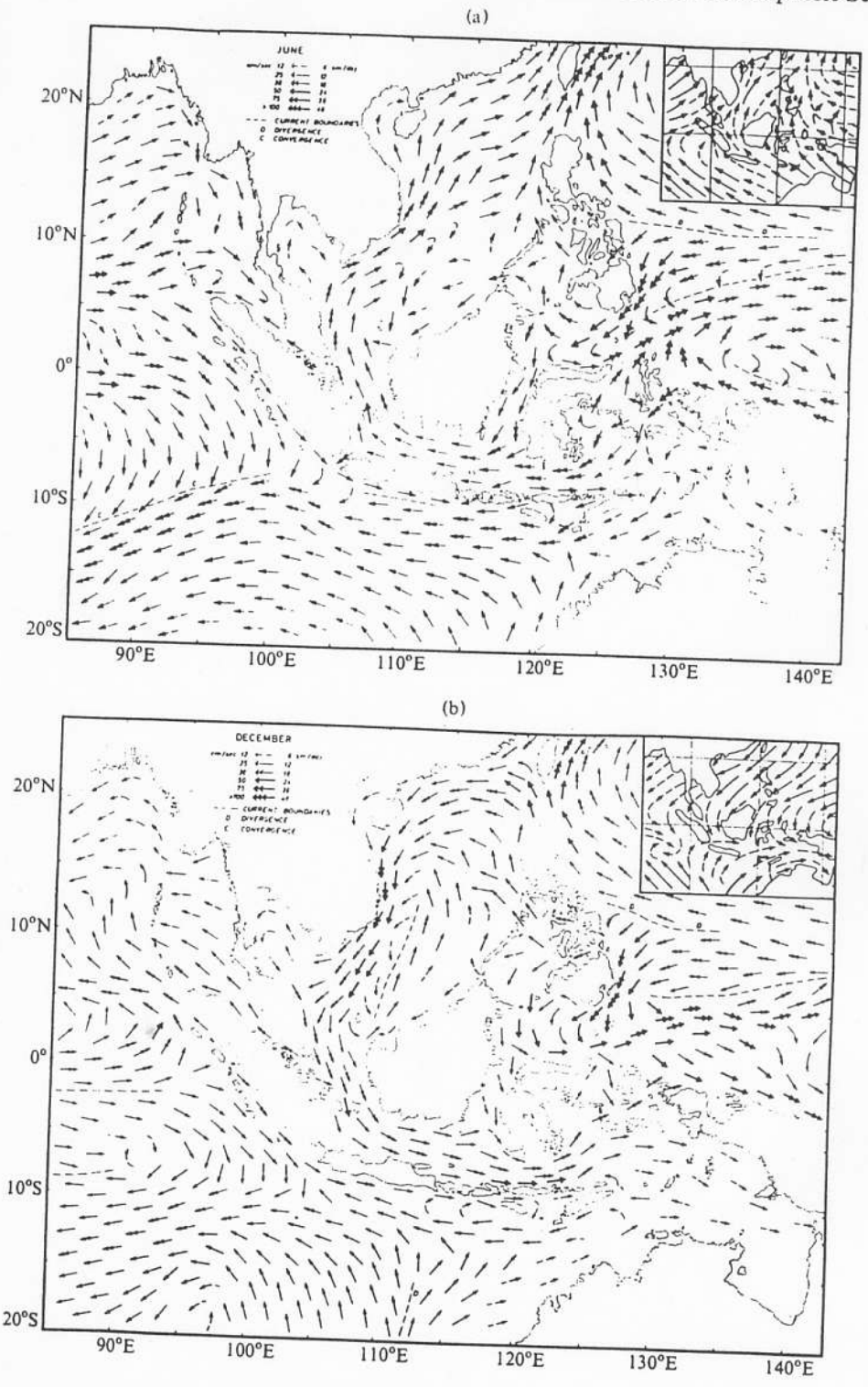


FIGURE 3. Observational surface circulation: (a) June, and (b) December (after Ref.[2]).

in summer, near Natuna Island and in reef areas. Large scale eddies have been found primarily during the summer monsoon[1]. Based on more complete data sets such as U.S. Navy's Master Oceanographic Observational Data Set (MOODS) and National Centers for Environmental Prediction (NCEP) monthly sea surface temperature (SST) data set, Chu et al.[5,6] identified multi-eddy structure in the SCS.

Upwelling and downwelling occur off the coast of central Vietnam and eastern Hainan. The summer monsoon is believed to cause an Ekman-type drift current and corresponding offshore transport, leading to upwelling[1]. Others[7] have pointed out that upwelling also occurs in these areas during winter monsoon conditions, casting doubt on previous ideas concerning the origin of these features.

In the north, the waters are cold and saline. The annual variability of salinity is small, due to the inflow and diffusion of high salinity water from the Pacific Ocean through the Bashi Channel. In the south the tropical conditions cause the waters to be warmer and fresher. The interface of the southern high temperature, low salinity water and the northern low temperature, high salinity causes a definite vertical gradient, usually strongest between 100 and 300 m deep. During the transitions the central region is alternately subjected to high and low salinity inflow as the monsoons reverse, resulting in a region of higher horizontal gradient and annual variability. Mixed layer depths vary from 30 to 40 m during the summer monsoon, and 70 to 90 m during the winter monsoon with variation due to both wind and current[2].

Three-dimensional ocean models have been used several times in the past to simulate the circulation in the SCS. Integrating a semi-implicit 12-layer shallow water model with 50 km resolution under both mean winter and summer conditions for 15 days, Pohlmann[8] simulated the reversal of the upper layer circulation between the summer and winter monsoon seasons. Integrating a 23-level primitive equation model developed at the Princeton University[9] with 20 km horizontal resolution under monthly mean climatological wind forcing[3] for a year, Chu et al.[10] simulated the seasonal variation of the SCS circulation and Chu and Chang[11] explained the formation of the SCS warm-core eddy in boreal spring. Integrating a global 1.5-layer reduced gravity model with 0.5° resolution, Metzger and Hurlburt[12] successfully simulated the upper layer circulation and the mass exchange between the SCS, the Sulu Sea, and the Pacific Ocean.

The objective of this study is to simulate the SCS thermohaline structure as well as the circulation and to investigate physical processes causing seasonal variability. We used the Princeton Ocean Model (POM) to examine the mechanisms causing seasonal variation of the SCS circulation and thermal structure. The control run is designed to best simulate reality against which each experiment is compared. In the experiments, various external and internal factors are modified and the resulting circulation patterns and magnitudes are compared to the control run results. Specifically we estimate the contribution (in terms of volume transport, sea surface elevation and circulation patterns) of non-linear advection, wind forcing and lateral boundary transport to the ocean features identified in the control results. From this we can estimate the relative importance of these factors to SCS oceanography.

## 2. THE NUMERICAL OCEAN MODEL

### 2.1 *Model Description*

Coastal oceans and semi-enclosed seas are marked by extremely high spatial and temporal variabilities that challenge the existing predictive capabilities of numerical simulations. The POM is a time dependent, primitive equation circulation model on a three-dimensional

grid that includes realistic topography and a free surface[9]. Tidal forcing was not included in this application of the model, since high frequency variability of the circulation is not considered. River outflow is also not included. However, the seasonal variation in sea surface height, temperature, salinity, circulation and transport are well represented by the model. From a series of numerical experiments, the qualitative and quantitative effects of non–linearity, wind forcing and lateral boundary transport on the SCS are analyzed, yielding considerable insight into the external factors affecting the region oceanography. The horizontal spacing of 0.179° by 0.175° (approximately 20 km resolution) and 23 vertical sigma coordinate levels. The model domain is from 3.06°S to 25.07°N, and 98.84°E to 121.16°E, which encompasses the SCS and the Gulf of Thailand, and uses realistic bathymetry data from the Naval Oceanographic Office DBDB5 database (5 minute by 5 minute resolution). Consequently, the model contains $125 \times 162 \times 23$ horizontally fixed grid points. The horizontal diffusivities are modeled using the Smagorinsky[13] form with the coefficient chosen to be 0.2 for this application. The bottom stress $\tau_b$ is assumed to follow a quadratic law

$$\tau_b = \rho_0 C_D |\mathbf{V}_b| \mathbf{V}_b, \tag{1}$$

where $\rho_0$ ($=1025$ kg / m$^3$) is the characteristic density of the sea water, $\mathbf{V}_b$ is the horizontal component of the bottom velocity, and $C_D$ is the drag coefficient which is specified as 0.0025 [9] in our model.

### 2.2 *Atmospheric Forcing*

The atmospheric forcing for the SCS application of the POM includes mechanical and thermohaline forcing. The wind forcing is depicted by

$$\rho_0 K_M \left( \frac{\partial u}{\partial z}, \frac{\partial v}{\partial z} \right)_{z=0} = (\tau_{0x}, \tau_{0y}, \tag{2}$$

where $(u, v)$ and $(\tau_{0x}, \tau_{0y})$ are the two components of the water velocity and wind stress vectors, respectively. The wind stress at each time step is interpolated from monthly mean climate wind stress[3], which was taken as the value at the middle of the month. The wind stress has a typical magnitude of 0.1–0.2 N / m$^2$ (Fig. 2). Over the two monsoon seasons the wind varies with location and time, leading to a complicated distribution of wind stress.

Surface thermal forcing is depicted by

$$K_H \frac{\partial \theta}{\partial z} = \alpha_1 \left( \frac{Q_H}{\rho c_p} \right) + \alpha_2 C(\theta_{\mathrm{OBS}} - \theta), \tag{3}$$

$$K_S \frac{\partial S}{\partial z} = \alpha_1 Q_S + \alpha_2 C(S_{\mathrm{OBS}} - S), \tag{4}$$

where $\theta_{\mathrm{OBS}}$ and $S_{\mathrm{OBS}}$ are the observed potential temperature and salinity, $c_p$ is the specific heat, and $Q_H$ and $Q_S$ are surface net heat and salinity fluxes, respectively. The relaxation coefficient $C$ is the reciprocal of the restoring time period for a unit volume of water. The parameters $(\alpha_1, \alpha_2)$ are (0, 1)–type switches: $\alpha_1 = 1$, $\alpha_2 = 0$, would specify only flux forcing being applied; $\alpha_1 = 0$, $\alpha_2 = 1$, would specify that only restoring type forcing is applied. In this study, the surface thermal forcing is determined solely by restoring forcing, that is $\alpha_1 = 0$ and $\alpha_2 = 1$ in Eqs. (3)–(4). The relaxation coefficient $C$ is taken to be 0.7 m / day, which is equivalent to a relaxation time of 43 days for an upper layer 30 m thick[14]. The net effect is to prevent any deviation from climatology and ensure that the SCS acts as a heat source.

### 2.3 *Lateral Boundary Forcing*

Closed lateral boundaries, i.e., the modeled ocean bordered by land, were defined using a

free slip condition for velocity and a zero gradient condition for temperature and salinity. No advective or diffusive heat, salt or velocity fluxes occur through these boundaries.

Open boundaries, where the numerical grid ends but the fluid motion is unrestricted, were treated as radiative boundaries. Volume transport through the Luzon Strait, Taiwan Strait, and Gasper / Karimata Strait was defined according to observations (Table 1). However, the Balabac Channel, Mindoro Strait, and Strait of Malacca are assumed to have zero transport. When the water flows into the model domain, temperature and salinity at the open boundary are likewise prescribed from the climatological data[15]. When water flows out of the domain, the radiation condition was applied,

$$\frac{\partial}{\partial t}(\theta, S) + U_n \frac{\partial}{\partial n}(\theta, S) = 0, \tag{5}$$

where the subscript $n$ is the direction normal to the boundary.

TABLE 1. Bi-monthly variation of volume transport (Sv) at the lateral open boundaries. The positive / negative values mean outflow / inflow and were taken from Ref.[2].

| Month | February | April | June | August | October | December |
|---|---|---|---|---|---|---|
| Gaspar–Karimata Straits | 4.4 | 0.0 | −4.0 | −3.0 | 1.0 | 4.3 |
| Luzon Strait | −3.5 | 0.0 | 3.0 | 2.5 | −0.6 | −3.4 |
| Taiwan Strait | −0.9 | 0.0 | 1.0 | 0.5 | −0.4 | −0.9 |

For the surface elevation, $\eta$, we use the radiation condition for the open boundary,

$$\frac{\partial \eta}{\partial t} + c\frac{\partial \eta}{\partial n} = F, \tag{6}$$

where $c$ is the local shallow water wave speed, and $F$ is the forcing term including tides. In this study, we use $F=0$.

### 2.4 *Initial Conditions and Initialization*

The model was integrated with all three components of velocity ($u$, $v$, $w$) initially set to zero, and temperature and salinity specified by interpolating climatology data[15] to each model grid point. The model year consists of 360 days (30 days per month), day 361 corresponds to 1 January. It was found that 90 days were sufficient for the model kinetic energy to reach quasi-steady state under the imposed conditions (Fig. 4). In order to first capture the winter monsoon to summer monsoon transition, the model was started from day 300 (30 October), and run to day 390 (30 January next year) for spin-up. After day 390, the model was run another 450 days for each experiment.

### 2.5 *Mode Splitting*

For computational efficiency, the mode splitting technique[9] is applied with a barotropic time step of 25 seconds, based on the Courant–Friederichs–Levy (CFL) computational stability condition and the external wave speed; and a baroclinic time step of 900 seconds, based on the CFL condition and the internal wave speed.

### 2.6 *Experiment Design*

Our approach was to carry out four numerical experiments: one control and three sensitivity runs. All runs were completed for the same 18 month period encompassing both summer and winter monsoons, and, except as specified below, utilized the same initial conditions (on day 300). Run 1 was the control run. The three sensitivity runs were: Run 2, linear

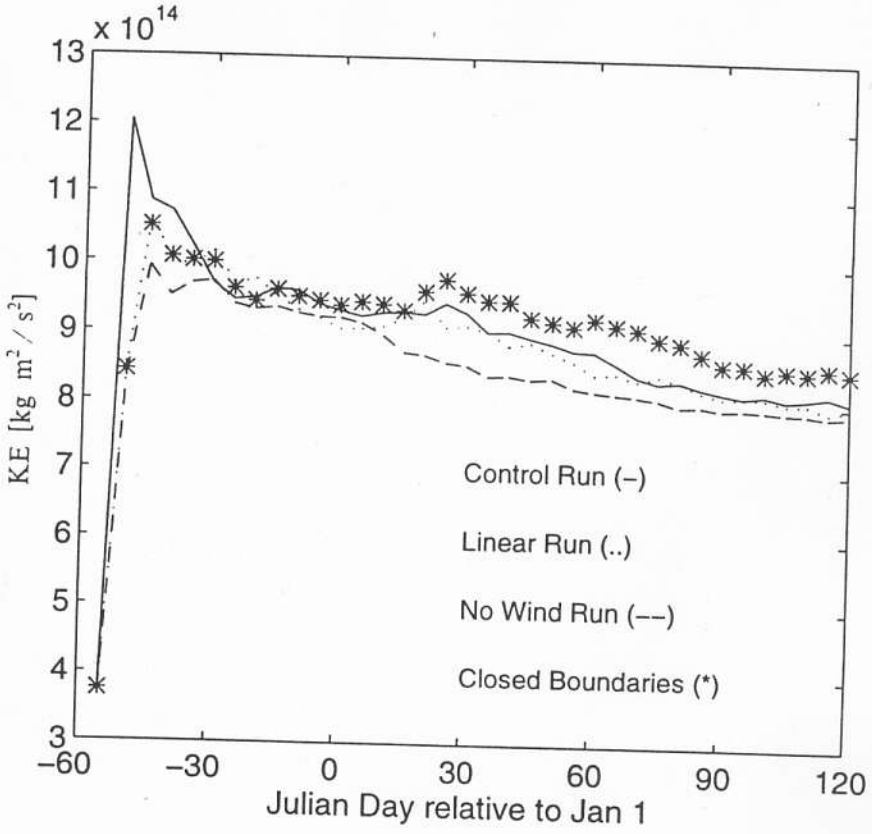


FIGURE 4. Temporal variation of total kinetic energy. The model is integrated from 1 November and reaches quasi–steady state after 90 days of integration.

dynamics; Run 3, no winds; Run 4, zero lateral transport at the open boundaries. The difference between the control and the sensitivity runs at each grid point and time should then isolate the nonlinear dynamics, wind forcing effect, and lateral boundary effect, enabling independent examination of each.

The thermohaline structure, sea surface elevation, circulation patterns, and volume transport that constitute the SCS oceanography will be identified from the control run for subsequent comparative analysis. An important assumption is made that the differences are linear, i.e., higher order terms and interactions are negligible and can be ignored, a *de facto* superposition. This assumption will be examined and qualified.

## 3. THE SIMULATION (CONTROL RUN)

### 3.1 *Circulation*

The most obvious feature of both the summer and winter SCS circulation, measured and modeled, is the western boundary current, the Vietnam Coastal Jet (VCJ). Hinted at in Wyrtki's depiction but more explicit in our model are the cross–basin currents located at 11–14°N. The model simulates both the summer and winter SCS circulation quite well compared to the observational study[2].

During the summer monsoon period (mid–May to August) winds blow from the southwest and the SCS surface (we refer to $z=0$) circulation generally follows suit with anticyclonicity in the southern basin (Figs. 5a–5c). Inflow is through the southern Gaspar and Karimata Straits and outflow is through the northern Taiwan Strait and eastern Bashi Chanel (Table 1). The simulated summer (June–August) mean general circulation pattern has the following features. Velocities reach 1 m / s at the peak of the summer monsoon within the Vietnam Coastal Jet (VCJ). The western boundary current splits into two currents at 12°N: the coastal current and off–shore current. The off–shore current further bifurcates into northward and southeastward branches. The bifurcation point is along 110°E at 14°N in May, and southward shifts to 10°N in July. The cross basin zonal current reaches 14°N with a core speed of 0.3 m / s in May and shifts to 12°N with a core speed of 0.6 m / s in July. The

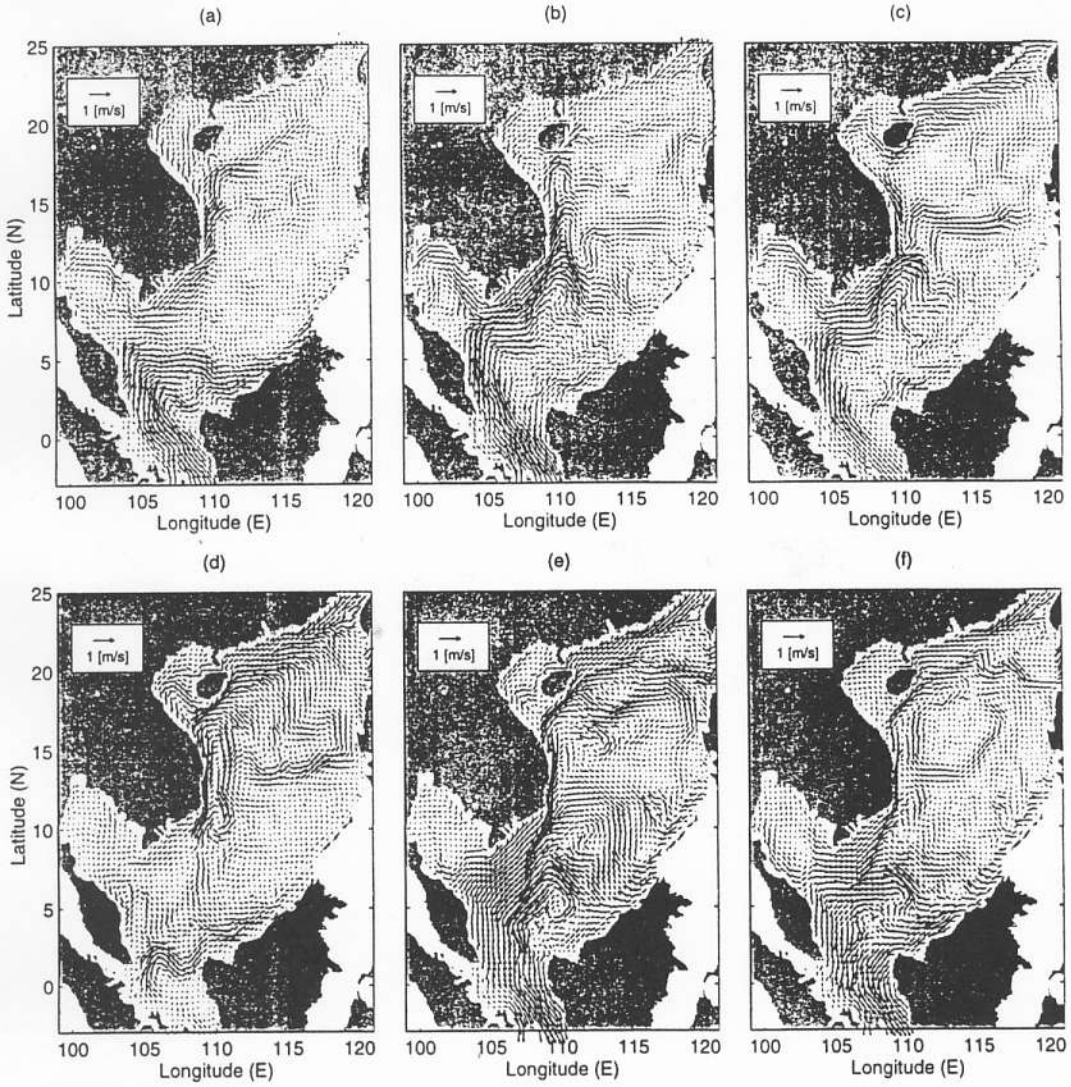


FIGURE 5. Surface circulation for control run on (a) May 15; (b) July 15; (c) September 15; (d) October 15; (e) December 15; and (c) March 15.

coastal branch continues north then east at Hainan Island. Such a VCJ summer bifurcation was simulated using a barotropic model[16,17].

During the winter monsoon period (November to March) the winter Asian high pressure system brings strong winds from the northeast and the SCS surface circulation pattern is cyclonic (Figs. 5d–5f). Inflow from the Bashi Channel (the Kuroshio intrusion) and Strait of Taiwan augments currents southwest along the Asian continental shelf, then south along the coast of Vietnam and eventually out through the Gasper and Karimata Straits in the south. Western intensification of the general cyclonic circulation pattern was also simulated. From the south coast of Hainan Island, the current intensifies as it flows from north to south along the Vietnam coast. Average speed is around 0.8 m / s in the core. As winter progresses, near surface currents along the coast of Borneo begin to turn northwest, eventually flowing directly away from the coastline and into the Natuna eddy where the southern edge of the deep basin meets the Sunda Shelf (Fig. 5e); the south extension of the VCJ veers west. In early spring a northward surface current developed adjacent to the VCJ (Fig. 5f) and persists through the transition periods to the start of the summer monsoon.

In order to compare the difference of the two monsoon seasons, we averaged the model variables such as velocity, surface elevation, temperature, and salinity over the two periods: June–August (summer) and December–February (winter.) The surface circulations for the summer (Fig. 6a) show an anticyclonic gyre in the deep basin with the VCJ flowing northward to northeastward. The winter circulations (Fig. 6b) indicate a reverse pattern: a cyclonic gyre in the deep basin with the VCJ flowing southward to southeastward. The seasonal variation of VCJ is illustrated by the zonal cross–sections of $v$–component at 13°N for winter (December –February) and summer (June – August). The summer VCJ is flowing northward with a mean maximum speed of 0.5 m / s and a width of 100 km, extending to a depth of around 200 m (Fig. 7a). The winter VCJ is a much stronger southward–flowing boundary current with a

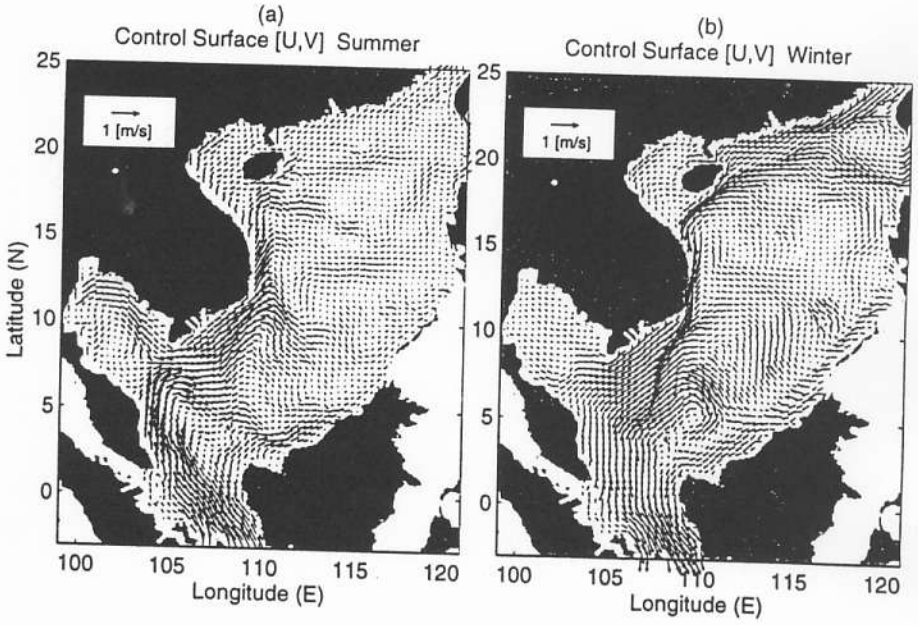


FIGURE 6. Mean surface circulation for control run during (a) summer, and (b) winter.

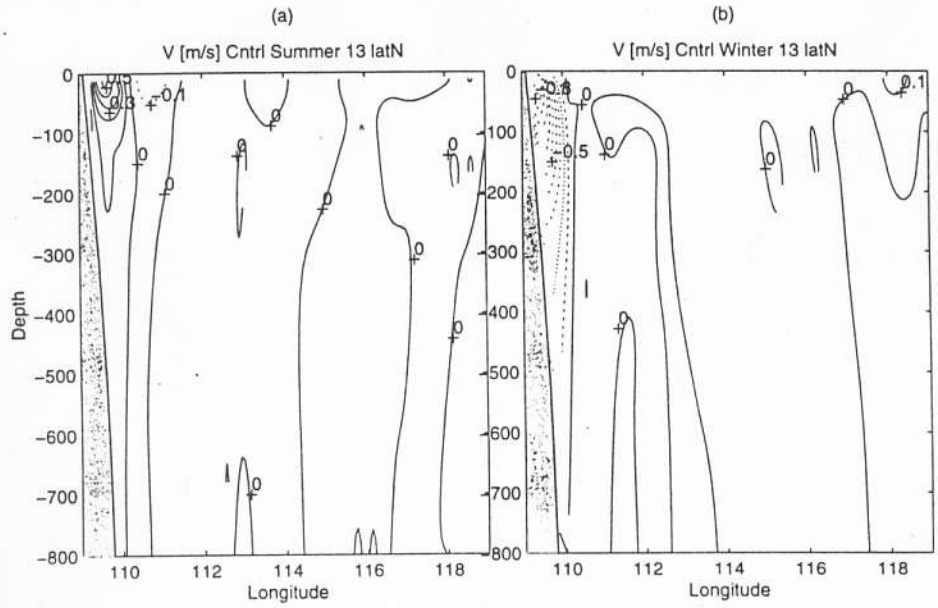


FIGURE 7. Mean latitudinal velocity for control run at the 13°N cross–section during (a) winter, and (b) summer.

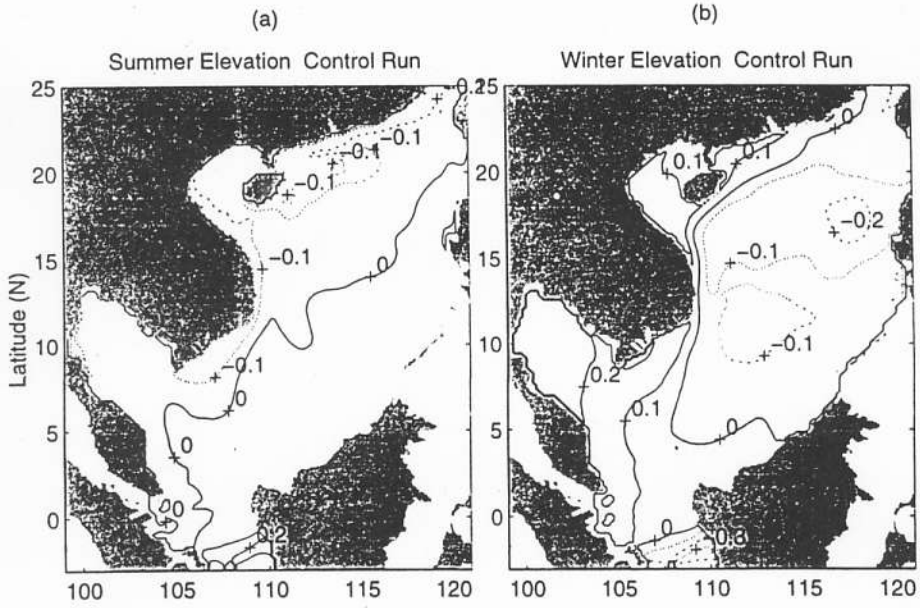


FIGURE 8. Mean surface elevation (m) for control run during (a) summer, and (b) winter.

mean maximum velocity of 0.95 m / s and a width of 100 km, extending to a depth of 500 m (Fig. 7b).

Sea surface heights for the winter show a 0.2 m depression over the deep basin with positive height in the south over the Sunda Shelf and the Gulf of Thailand (Fig. 8a). Average summer sea surface elevation varies from −0.1 to 0.1 m with a southeast upward tilt (Fig. 8b).

### 3.2 *Thermohaline Structure*

Isotherms and isohalines for summer and winter are nearly horizontal from east to west except at the coastal regions (Fig. 9). Localized lifting of the isotherms and isohalines during summer at the west boundary indicates coastal upwelling inside the VCJ (Figs. 9a and 9c). Localized descending of the isotherms and isohalines during winter at the west boundary indicates coastal downwelling inside the VCJ (Figs. 9b and 9d). Both coastal upwelling and downwelling, combined with the high velocity shear across the VCJ, result in baroclinic instability.

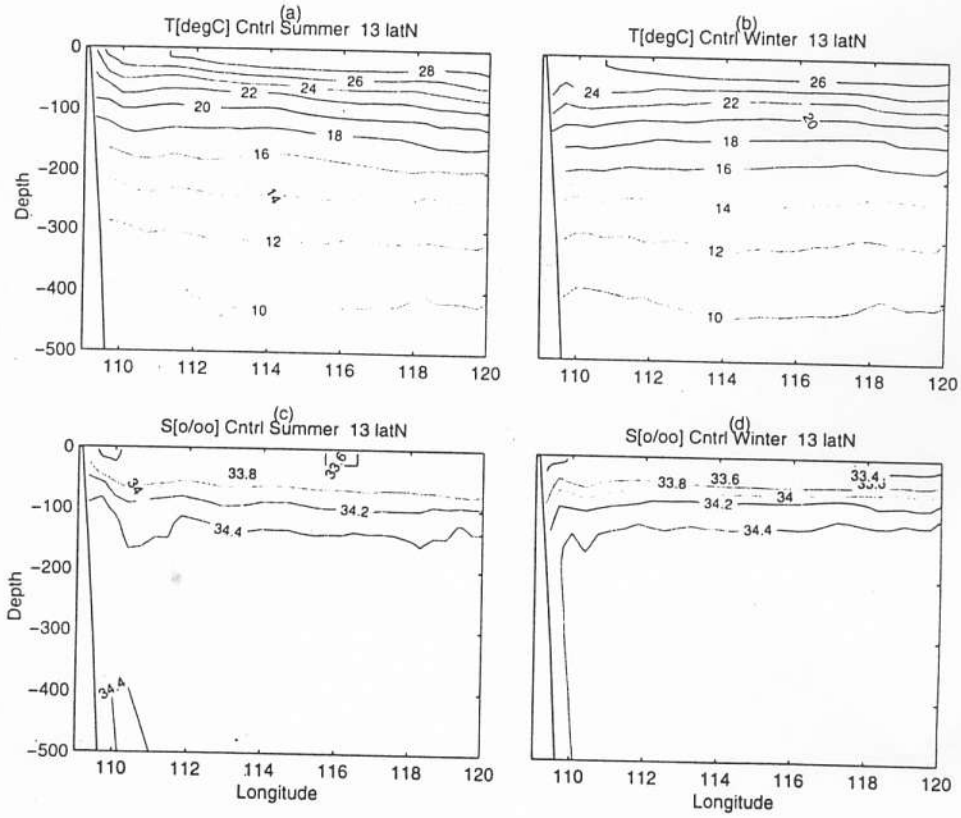


FIGURE 9. Thermohaline feature at the 13°N zonal cross–section simulated by the control run: (a) summer temperature (°C); (b) winter temperature (°C); (c) summer salinity (psu), and (d) winter salinity (psu).

Latitudinal thermohaline variation for summer and winter is shown in Fig.10. In general model thermohaline structure is consistent with the two SCS water masses described by Wyrtki[2]. Over the southern basin there is a general lifting of isotherms of 40–50 m from winter to summer above 200 m. In the northern SCS, near–surface waters (20–50 m) are influ-

enced by the winter inflow of North Pacific Kuroshio water. They are uniformly colder and more saline and there is a weaker thermocline in winter than in summer. In the south the equatorial climate and summer inflow from the shallow Java Sea cause the water mass to be fresher, warmer with a slightly deeper thermocline. The model SCS summer thermocline depth is in good agreement with Ref. [2], at 30 and 50 m, as opposed to the model winter depth which is much shallower.

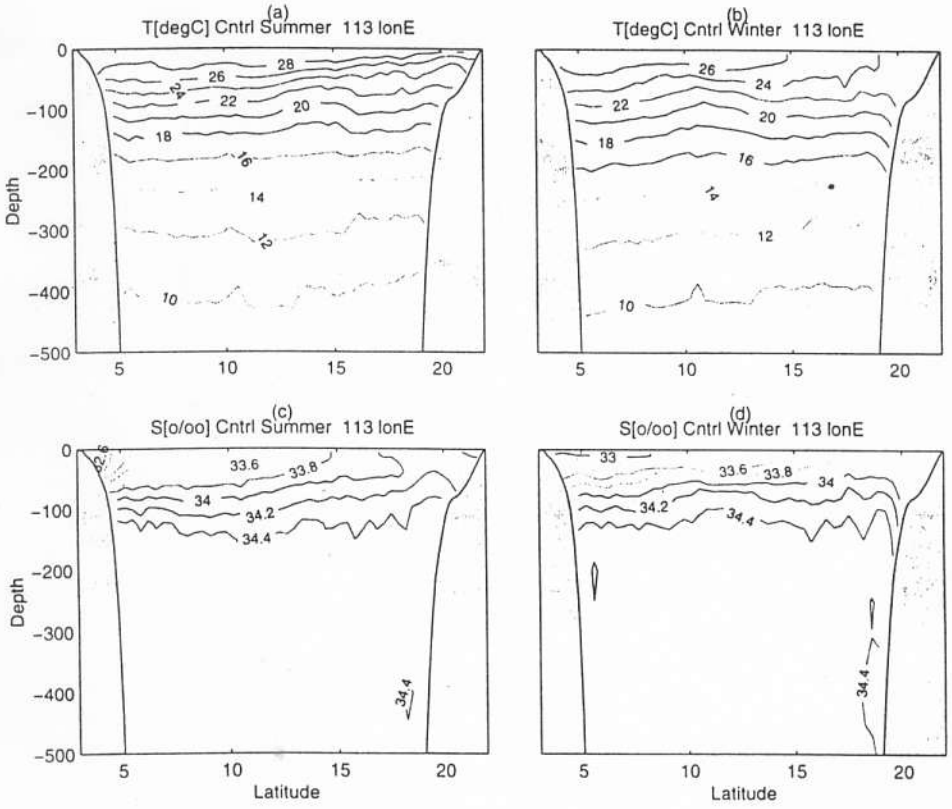


FIGURE 10. Same as Fig.9 except for the 113°E latitudinal cross–section.

### 3.3 *Volume Transport*

The volume transport stream functions for summer and winter are shown in Figs. 11a and 11b. For the SCS deep basin, the barotropic flow reveals an anticyclonic (cyclonic) gyre in the summer (winter). For the SCS continental shelf / slope regions, the volume transport has an evident seasonal variation. Winter volume transport is strongest along the north and west slope with significant eddy and meander activity, and across the southern slope of the deep basin. Average winter VCJ transport is about 10.6 Sv. Summer shows a weaker VCJ transport (5.5 Sv) with similar transport along the southern slope of the deep basin, again with noticeable eddy activity (Table 2).

### 3.4 *Natuna Island Eddy*

During winter, the confluence of the VCJ and the offshore flow from Borneo in the

TABLE 2. Volume transport (Sv) of individual features simulated by the control run.

| Feature | Transport |
|---|---|
| Summer Vietnam Coastal Jet | 5.5 |
| Winter Vietnam Coastal Jet | 10.6 |
| Natuna Island Eddy | 5.0 |

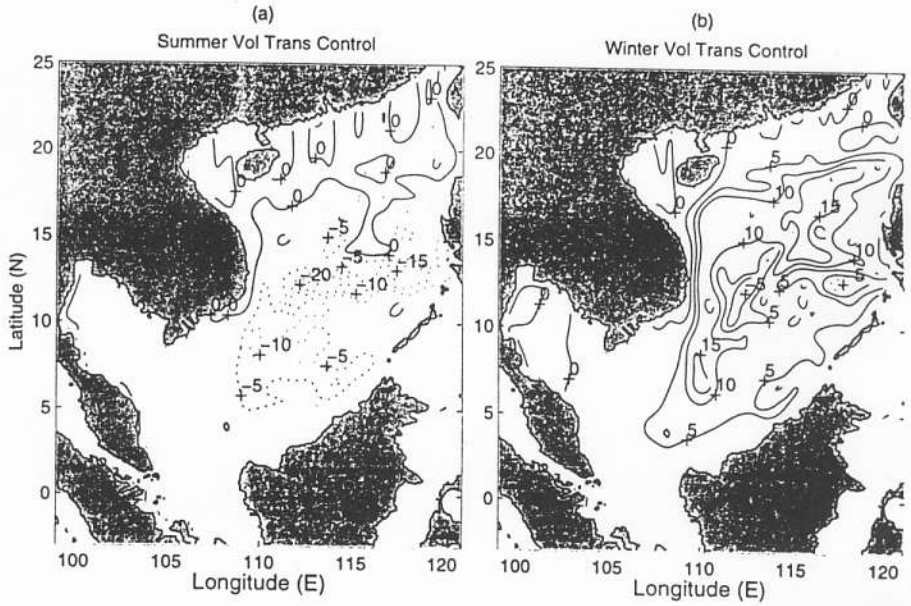


FIGURE 11. Mean total volume transport streamfunction (Sv) for control run during (a) summer, and (b) winter.

Sunda Shelf generates a mesoscale cyclonic eddy (Fig. 6b), here termed the Natuna Island Eddy (NIE), consistent with observations of late winter surface circulation described by Wyrtki (Fig. 3b). This eddy shows little variability during the winter, with maximum swirl velocity of 0.6 m / s at the peak of the winter monsoon but no variation in position. NIE is a weak anticyclonic eddy (Fig. 6a) during summer, and a strong cyclonic eddy (Fig. 6b) during winter. The summer NIE has an average core velocity of 0.1 m / s. The winter NIE has an average core velocity of 0.45–0.5 m / s. The east–west slanted eddy core is deeper on the west side (depth ~ 40 m) of the eddy than on the east side (depth ~ 20 m). The vertical shear of horizontal velocity promotes baroclinic instability.

## 4. DRIVING MECHANISMS

We analyzed the results of the four experiments to identify the driving mechanisms for the SCS circulation.

### 4.1 *Effects of Non–Linearity ( Run 1 – Run 2)*

In the first sensitivity study the nonlinear advection terms were removed from the

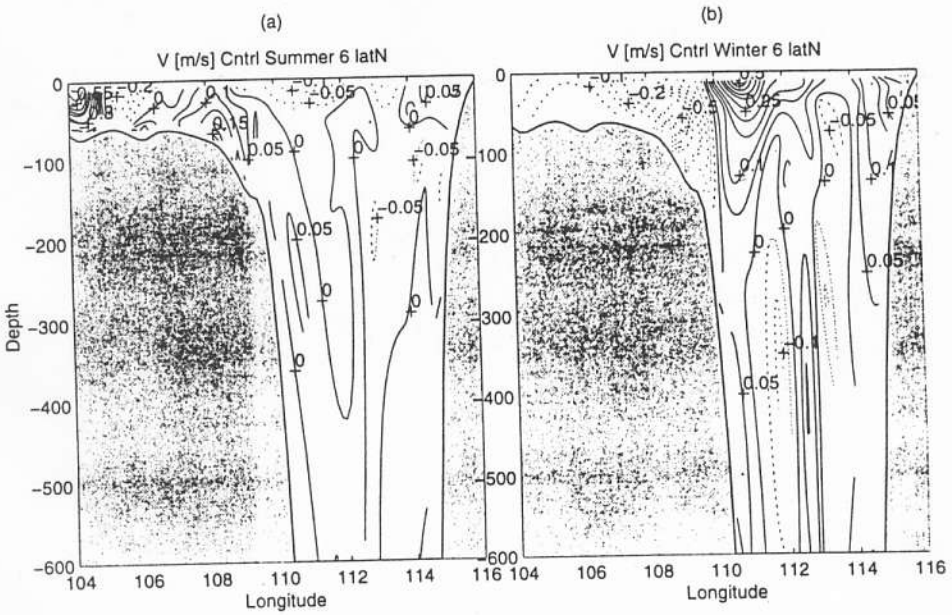


FIGURE 12. Mean latitudinal velocity for control run at the 6°N cross–section during (a) summer, and (b) winter.

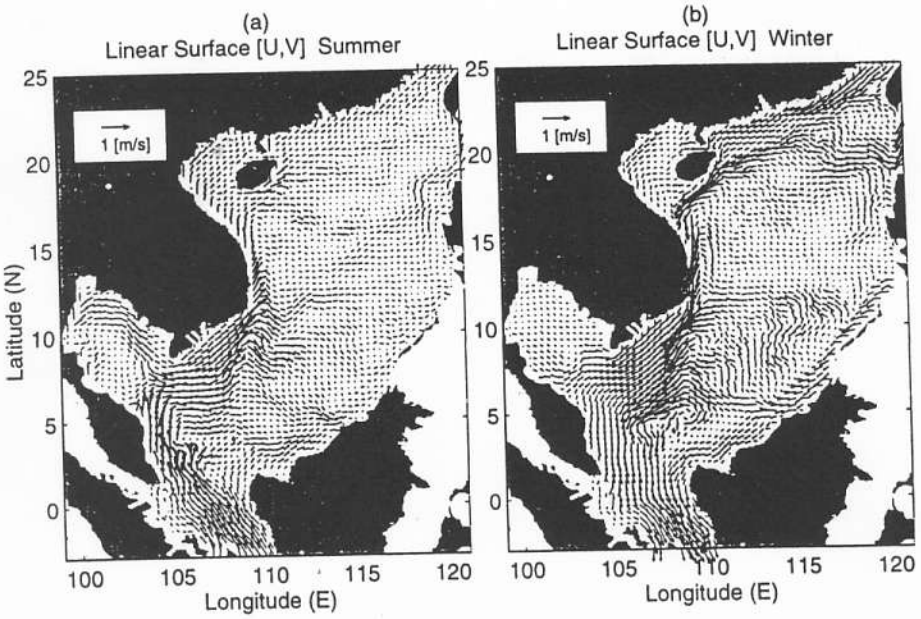


FIGURE 13. Mean surface circulation for linear run during (a) summer, and (b) winter.

dynamic equations. Otherwise the same parameters as the control run were used. The near surface vector velocities for the summer (Fig. 13a) and winter (Fig. 13b) illustrate the similarity to the control run results (Fig. 6), which indicates that the non–linearity does not change the general circulation pattern. However, our computation shows that the non–linearity causes a noticeable change in the volume transport and the strength of the western boundary currents.

Figs.14a and 15a are plots of the difference in the volume transport streamfunction ($\Delta\psi$) for the control run minus the linear run and represent nonlinear effects for summer and winter, respectively. The biggest $\Delta\psi$ during both seasons is a deep–basin double–gyre feature: an anticyclonic gyre (−5 Sv) west of Luzon and a cyclonic gyre (10 Sv) west of Liyue Bank (11°N, 115°E). Such a double–gyre structure indicates (a) a westward cross–basin transport (15 Sv) near 13°N (between the two gyres), (b) increase (decrease) of cyclonic (anticyclonic) transport in the southwestern basin (south of 13°N), and (c) increase (decrease) of anticyclonic (cyclonic) transport in the northeastern basin (north of 13°N). Furthermore, two nearly parallel zero curves of $\Delta\psi$ show up near the Vietnam coast during the summer (Fig. 14a). One curve is close to the coast, and the other curve is off shore. This shows that $\Delta\psi = 0$ on the entire Vietnam shelf, resulting in no change in the northward VCJ transport in the summer. While, during the winter such a feature ($\Delta\psi = 0$) appears only north of 13°N and some southward volume transport increment ($\Delta\psi = 4$ Sv) shows up near the Vietnam coast south of 13°N. After averaging $\Delta\psi$ over the Vietnam coast shelf break, we estimated that the nonlinear advection brings a 3.1 Sv of the VCJ.

The evident nonlinear effect on the western boundary current can be identified by the velocity difference for the control run minus the linear run. A cross–section of the latitudinal velocity difference during the summer at 6°N shows that nonlinear advection augments coastal

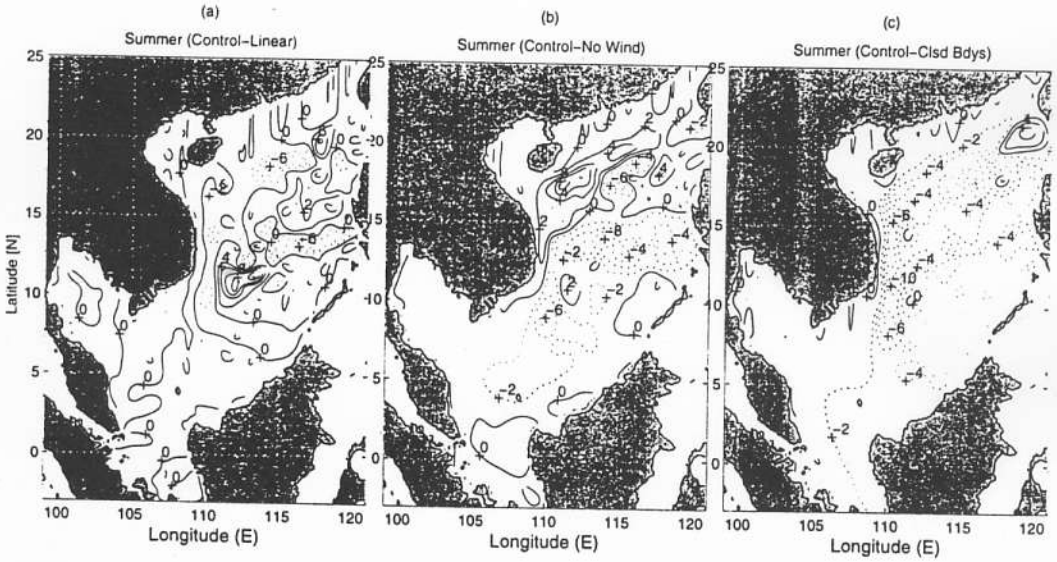


FIGURE 14. Summer volume transport anomaly (Sv) caused by effects of (a) nonlinearity; (b) winds; and (c) boundary forcing.

core current at the western boundary by about 0.25 m / s and is responsible for offshore eddy activity (Fig. 16a). Such a nonlinear effect was also found in the surface velocity vector difference ($\Delta V$) field. The primary feature of the nonlinear effect on circulation during the winter (Fig. 17a) is similar to that during the summer (Fig. 18a): quite evident near the west coast and not evident elsewhere.

4.2 *Wind–Induced Circulation ( Run 1 −Run 3)*

The difference between Run 1 and Run 3 shows the monsoon wind effects on the SCS

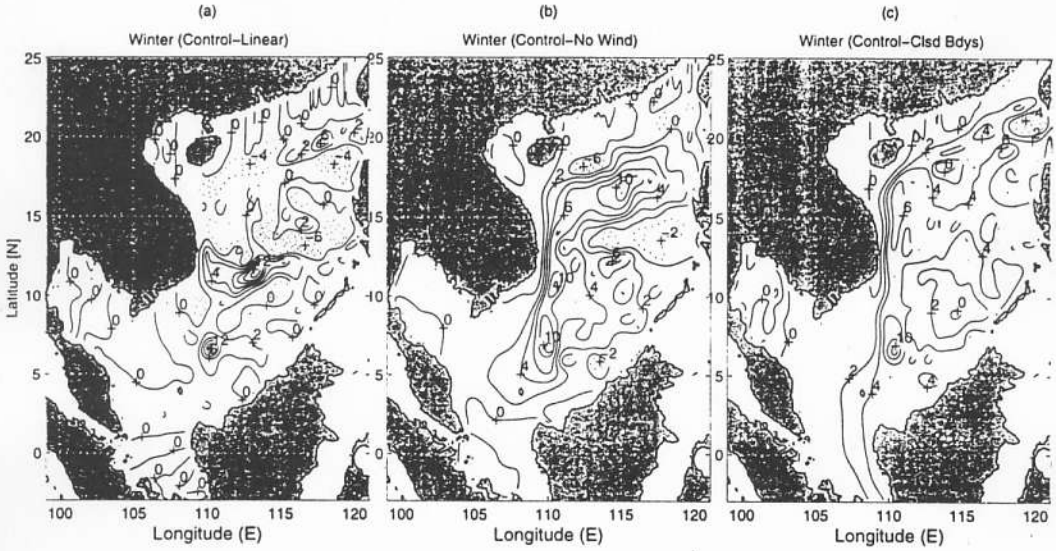


FIGURE 15. Winter volume transport anomaly (Sv) caused by effects of (a) nonlinearity; (b) winds; and (c) boundary forcing.

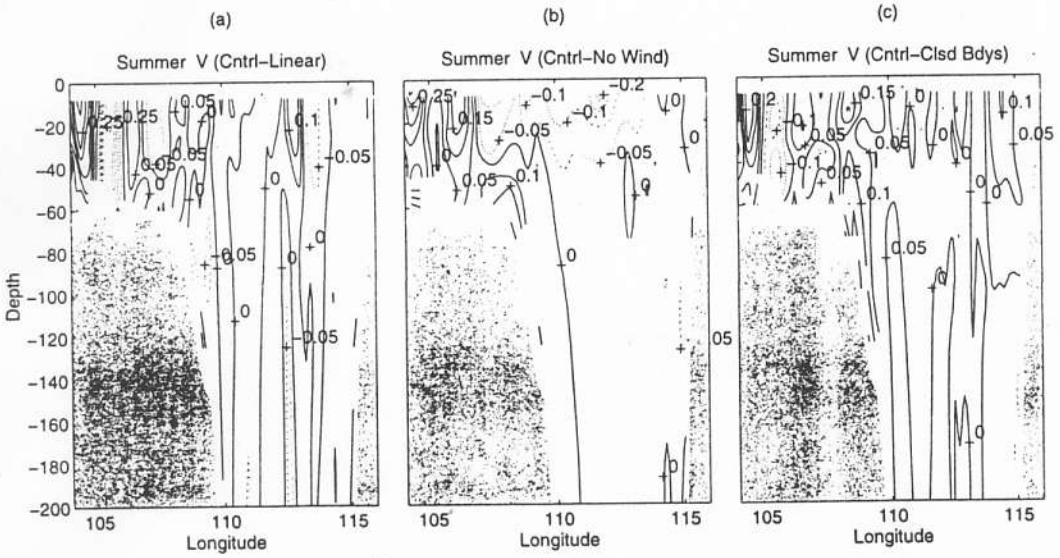


FIGURE 16. Summer latitudinal velocity anomaly (m / s) at the 6°N cross–section, caused by effects of (a) nonlinearity, (b) winds, and (c) boundary forcing.

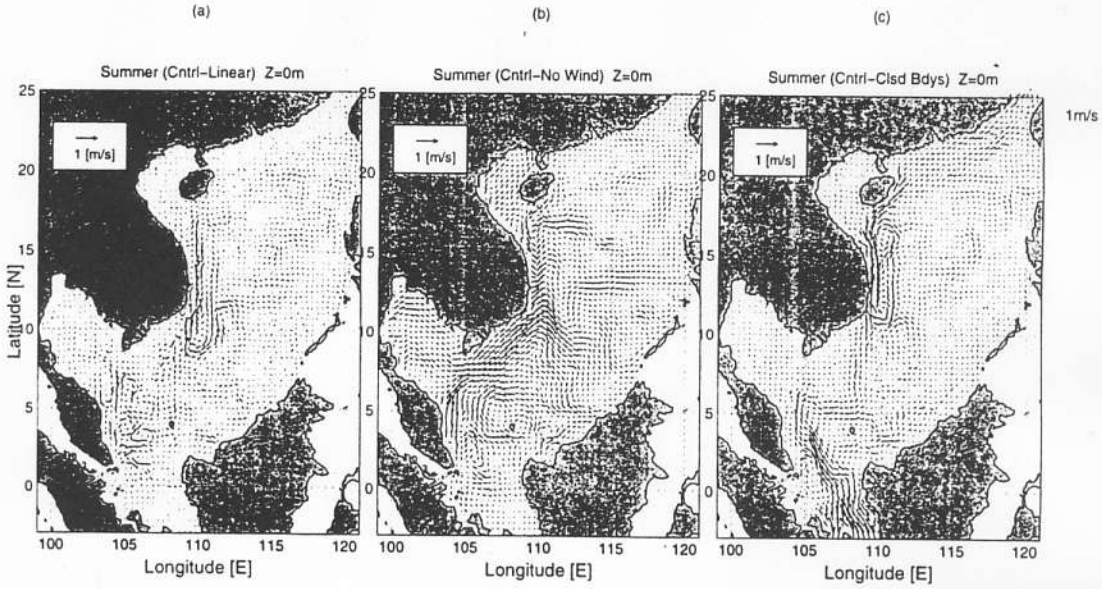


FIGURE 17. Summer surface current anomaly caused by effects of (a) nonlinearity, (b) winds, and (c) boundary forcing.

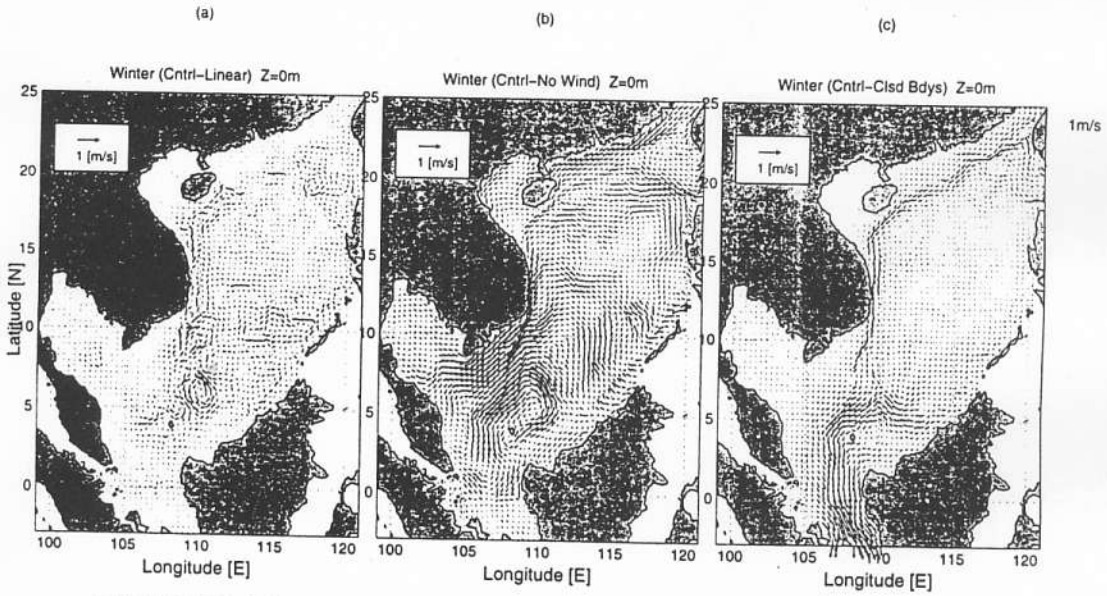


FIGURE 18. Winter surface current anomaly caused by effects of (a) nonlinearity, (b) winds, and (c) boundary forcing.

surface circulation and SST for the summer and winter respectively. The primary feature of the summer wind effect (Fig. 17b) on circulation and volume transport is in contrast to the winter wind forcing (Fig. 18b). The winter wind forcing causes the cyclonic gyre northeast Natuna Island (the NIE) with an average 0.3–0.4 m / s rotational velocity, the cross–basin flow and the connecting loop across the Sunda shelf around Natuna Island. The winter VCJ

flows with 0.3–0.4 m / s velocity (Fig. 18b) corresponding to a southward volume transport of 4.6 Sv (Fig. 15b). The China slope flow is actually slightly more than the control run but this may be accounted for by nonlinearity. When winds are removed from the forcing, the model results show considerable change in the structure of the summer circulation and a virtual disappearance of features in the winter circulation (note similarities in Figs. 6b and 18b); surface velocities are reduced by 0.20–0.3 m / s.

The summer winds drive a mesoscale anticyclonic eddy near a shallow depression in the Sunda shelf and Natuna Island, with rotation speeds of 0.15–0.2 m / s (Fig. 16b.) Winds also induce the loop current joining the Sunda shelf flow and the VCJ, bifurcation of the coastal current, and cross–basin flow (Fig 17b.) The corresponding wind effect on summer volume transport is largely limited to the northern SCS (Fig.14b) with a 6–8 Sv maximum transport along the China slope and a 4–6 Sv eastward transport centered on 13°N, a region of significant nonlinear effect.

Summer wind reduces SST slightly (1–2°C ) from upwelling off central and northern Vietnam and the east coast of Hainan (Fig. 19a). Winter wind decreases surface temperature to a lesser extent on the east side of the basin along the Palawan Trough (Fig. 19b).

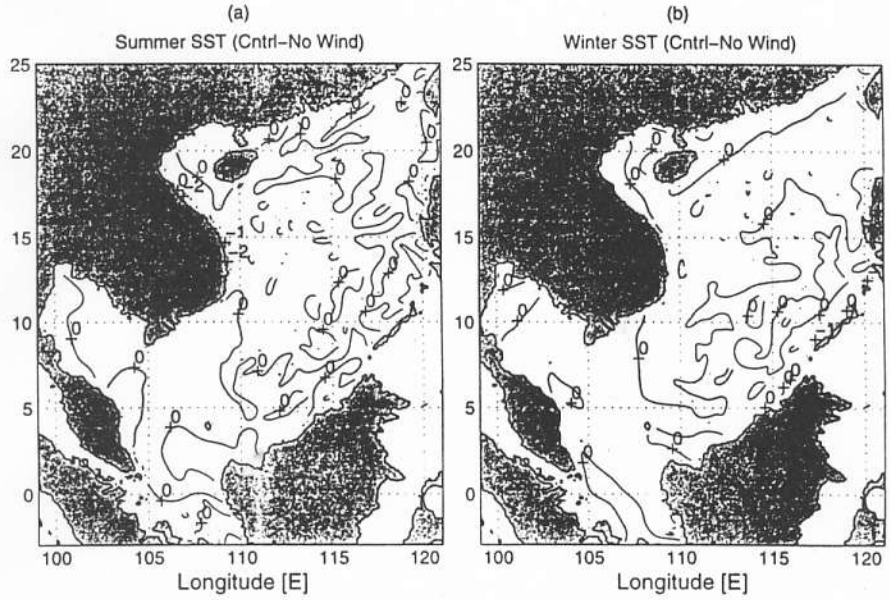


FIGURE 19. Sea surface temperature anomaly caused by wind effect.

Summer winds shift the average surface elevation to the north, increasing the elevation 5–10 cm, while elsewhere decreasing the height by the same magnitude (Fig. 20b). The winter wind increases the surface elevation over the continental shelves by 0.15–0.18 m, and decreases the elevation over the deep basin (Fig. 21b).

### 4.3 *Inflow/ Outflow Induced Circulation ( Run 1 – Run 4)*

The third sensitivity study used the control run equations and forcing but closed all open lateral boundaries, preventing transport of mass, heat or salinity through the Luzon Strait, Taiwan Strait or Gasper and Karimata Straits. With no inflow or outflow the summer anticyclonic gyre and winter cyclonic gyre are more pronounced. Increased recirculation generally leads to greater horizontal and vertical variability of the current structure.

The results for summer lateral boundary–forcing retain more of the anticyclonic nature of the circulation than do those from wind–forcing, see volume transport streamfunction difference $\Delta\psi$ (Figs. 14b and 14c.) The flow is generally slope hugging. The largest gradient of $\Delta\psi$ is located off South Vietnam (Fig. 14c), causing the strong western boundary currents. The southern inflow splits south of Natuna Island and fans across the Sunda shelf, forming a small anticylonic eddy collocated with that forced by the summer wind. The VCJ transports 5.5 Sv and is accompanied by a counter current nearby. At 6°N (Fig. 16c), however, notice that the average northward velocity throughout most of the shallow shelf region shows no discernible pattern of change, while the shelf current along the 100 m isobath decreases by 0.05–0.1 m / s. The summer circulation patterns change dramatically when the lateral boundary transport is removed. This can be seen from the surface velocity vector difference $\Delta V$ (Fig.17c). There is still western intensification of current along the coast of Malaysia, and it still joins the flow out of the Gulf of Thailand to contribute to an intensification of current off southern Vietnam.

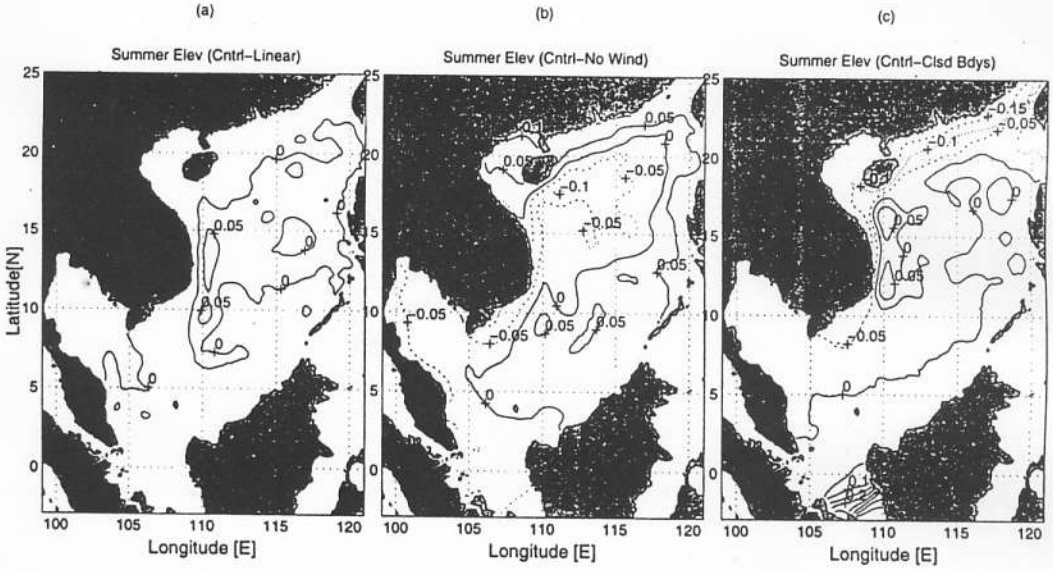


FIGURE 20. Summer surface elevation anomaly (m) caused by effects of (a) winds, and (b) boundary forcing.

Winter closed boundary circulation patterns on the other hand, show less difference in structure from the control run but more variability in magnitude. There is an average decrease of 0.1–0.4 m / s in current speed of the winter VCJ (Fig. 15c), which equates to 4–6 Sv southward volume transport. The positive wind curl acts to strengthen the cyclonic gyre nature of overall circulation. The Kuroshio intrusion and inflow through the Taiwan Strait are obviously supplemented by recirculation flow from along the coast of Luzon Island. Near Natuna Island it is noteworthy that the structure of cross–basin circulation and current flow away from the Borneo coast are unchanged. Similarly, it is apparent that the spatial extent and shape of the gyre northeast of Natuna Island is unchanged by closing the boundary flow. In cross section, however, it can be seen that the NIE does lose some of its velocity —there is a 0.1–0.3 m / s decrease in the average core velocity on the western side at 6°N in this run corresponding to a volume transport of 3 Sv, associated with the decrease in velocity of the VCJ. The difference in velocity is much smaller on the eastern side, suggesting that some other ef-

fect dominates the current structure in that region.

The nonlinearity increases the surface elevation slightly (0.05 m) near the south Vietnam coast in summer (Fig. 20a), and has almost no effect on the surface elevation in winter (Fig. 21a). The summer lateral boundary transport decreases the average surface elevation over the China–Vietnam continental shelf by 0.05–0.15 m, while elsewhere increases the height with a maximum accretion of 0.2–0.4 m near the Karimata Strait (Fig. 20c). The winter lateral boundary transport increases the average surface elevation over the China–Vietnam continental shelf by 0.05–0.2 m, while elsewhere decreases the height with a maximum reduction of 0.25 m near the Karimata Strait (Fig. 21c).

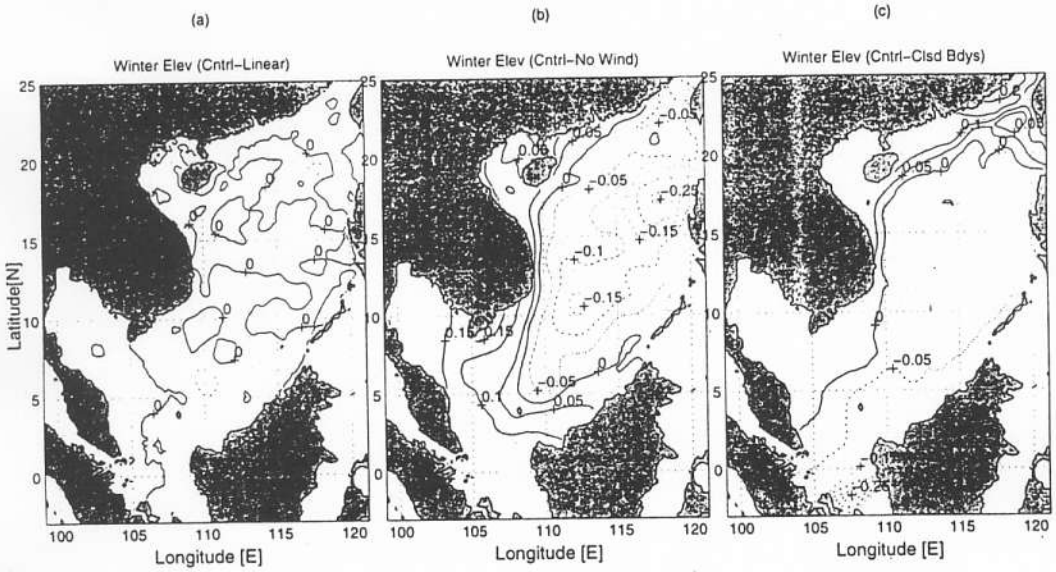


FIGURE 21. Winter surface elevation anomaly (m) caused by effects of (a) winds, and (b) boundary forcing.

## 5. CONCLUSIONS

(1) The SCS circulation and thermohaline structure were simulated in this study by the POM model under the climatological forcing. During summer (winter) monsoon period the SCS surface circulation is generally anticyclonic (cyclonic) with a strong western boundary current (width around 100 km) – Vietnam Coastal Jet. This jet has a strong seasonal variation and flows northward (southward) during summer (winter) with a mean maximum speed of 0.5 m / s (0.95 m / s), mean volume transport of 5.5 Sv (10.6 Sv), extending to a depth of around 200 m (500 m). During summer, the western boundary current splits and partially leaves the coast; the bifurcation point is at 14°N in May, and shifts south to 10°N in July. The cross–basin zonal current reaches 12°N and a core speed of 0.6 m / s by the end of the summer. The coastal branch continues north then east at Hainan Island. Average summer sea surface elevation varies from −0.1 to 0.1 m with a southeast upward tilt. Sea surface heights for the winter show a 0.2 m depression over the deep basin with positive height in the south over the Sunda Shelf and the Gulf of Thailand. Besides, the POM model successfully simulates a mesoscale eddy in the Sunda Shelf, that is the Natuna Island Eddy. This eddy is cyclonic (anticyclonic) with maximum swirl velocity of 0.6 m / s at the peak of the winter monsoon.

Isotherms and isohalines for summer and winter are nearly horizontal from east to west except at the coastal regions. Coastal upwelling and downwelling are also simulated: localized lifting (descending) of the isotherms and isohalines during summer (winter) at the west boundary. Both coastal upwelling and downwelling (causing horizontal thermohaline gradient), combined with the high velocity shear across the coastal jet, result in baroclinic instability. This mechanism may contribute to the summer jet bifurcation. In general model thermohaline structure is consistent with the two SCS water masses described by Wyrtki[2]. Over the southern basin there is a general lifting of isotherms of 40–50 m from winter to summer above 200 m. In the northern SCS, near–surface waters (20–50 m) are influenced by the winter inflow of North Pacific Kuroshio water.

(2) The model nonlinear effects on circulation in the summer SCS are localized. There is a dipole in volume transport over the western corner of the southern slope of the deep basin in conjunction with anticyclonic transport extending across the mid–basin above this southern slope. The winter mid–basin transport is similarly anticyclonic but with the dipole reducing to a single cyclonic center and the addition of another cyclonic transport center near Natuna Island. The mid–basin transport and winter cyclonic center have a weak surface current signature. The winter surface current for nonlinear dynamic effects clearly shows the NIE. Elevation is little effected by nonlinear dynamics.

(3) The model wind effects on the SCS are more perversive than those of non–linear dynamic effects. Similar to nonlinear effects there are areas of anticylonic volume transport mid–basin in the summer and winter, although the mid–basin surface currents reverse. Summer wind effects on transport are generally divided along the axis of the monsoon wind, SW to NE, with anticyclonicity and positive elevation in the southeast and cyclonic transport and negative elevation in the northwest. Winter wind effect is largely cyclonic, including a center (with a strong surface current signature) for the NIE, with a matching steeper depression in surface elevation.

(4) The model boundary–forcing effect on volume transport is most easily distinguished as anticyclonic in the summer and cyclonic in the winter. The stronger transport centers of both seasons have strong surface current signatures including the NIE. Topographically linked eddy flow and transport are evident in the summer while winter flow narrowly follows the 200 m isobath until it encounters the Sunda Shelf and Natuna Island.

In the summer SCS volume transport is mostly due to boundary–forcing. Surface movement is marginally dominated by wind–forcing, when the boundary–forcing surface effect (away from the southern boundary) coalesces with associated volume transport. Winds drive the offshore summer bifurcation of the VCJ. The anticylonic gyre south of Hainan is a surface phenomenon driven by boundary–flow interaction with topography and nonlinear dynamics.

In the winter surface movement due to boundary–forcing is largely limited to the perimeter of the SCS basin, specifically a narrow swath over the 200 m isobath, away from the southern boundary. Surface flow and volume transport are dominated by wind effect except at the NIE, a mesoscale feature that must be qualified by nonlinear dynamics. Also to be qualified by nonlinear dynamics is cross–basin transport for both seasons. Further consideration of cross–basin transport should accommodate flow through the Mindoro Strait. Inspection of observational surface currents from the Sulu Sea shows that these flows may be important to formation of the two gyre system that exists in the spring.

(5) Future studies should concentrate on less simplistic scenarios. Realistic surface heat and salt fluxes should be included and the use of extrapolated climatological winds needs to be upgraded to incorporate synoptic winds to improve realism. Finally, the assumption of quasi–linearity that allowed us to use simple difference to quantify the effect of external forc-

ing needs to be rigorously tested. It is very important to develop a thorough methodology to perform sensitivity studies under the highly non–linear conditions that may exist in the littoral environment.

## ACKNOWLEDGMENTS

The authors wish to thank George Mellor and Tal Ezer of the Princeton University for most kindly proving us with a copy of the POM code and to thank Laura Ehret and Chenwu Fan for programming assistance. This work was funded by the Office of Naval Research NOMP Program, the Naval Oceanographic Office, and the Naval Postgraduate School.

## REFERENCES

[1] Huang, Q. and W. Wang, 1994: Current characteristics of the South China Sea, in: *Oceanology of China Seas*, edited by Z. Di, L. Yuan–Bo, and Z. Cheng–Kui, Kluwer, Boston, 39–46.

[2] Wyrtki, K., 1961: Scientific results of marine investigations of the South China Sea and the Gulf of Thailand 1959–1961. *Naga Report*, Vol.2, University of California at San Diego, 195pp.

[3] Hellerman, S. and M. Rosenstein, 1983: Normal monthly wind stress over the world ocean with error estimates. *J. Phys. Oceanogr.*, **13**, 1093–1104.

[4] Hu, J. and M. Liu, 1992: The current structure during summer in southern Taiwan Strait. *Tropic Oceanology*, **11**, 42–47.

[5] Chu, P.C., H.–C. Tseng, C.P. Chang, and J.M. Chen, 1997: South China Sea warm pool detected in spring from the Navy's Master Oceanographic Observational Data Set (MOODS). *J. Geophys. Res.*, **102**, 15761–15771.

[6] Chu, P.C., S.–H. Lu, and Y.–C. Chen, 1997: Temporal and spatial variabilities of the South China Sea surface temperature anomaly. *J. Geophys. Res.*, **102**, 20937–20955.

[7] Chen, J., Z. Fu and F. Li, 1982: A study of upwelling over Minnan–Taiwan shoal fishing ground. *Taiwan Strait*, **1**, 5–13.

[8] Pohlmann, T., 1987: A three–dimensional circulation model of the South China Sea. in: *Three–Dimensional Models of Marine and Estuarine Dynamics*, edited by J. Nihoul and B. Jamart, 245–268, Elsevier–Science Publishing Co., Amsterdam.

[9] Blumberg, A. and G. Mellor, 1987: A description of a three–dimensional coastal ocean circulation model, *Three–Dimensional Coastal Ocean Models*, edited by N.S. Heaps, American Geophysics Union, Washington D.C., 1–16.

[10] Chu, P.C., C.C. Li, D.S. Ko, and C.N.K. Mooers, 1994: Response of the South China Sea to seasonal monsoon forcing, *Proceedings of the Second International Conference on Air–Sea Interaction and Meteorology and Oceanography of the Coastal Zone*, American Meteorological Society, Boston, 214–215.

[11] Chu, P.C., and C.P. Chang, 1997: South China Sea warm pool in boreal spring, *Adv. Atmos. Sci.*, **14**, 195–206.

[12] Metzger, E. J. and H. Hurlburt, 1996: Coupled dynamics of the South China Sea, the Sulu Sea, and the Pacific Ocean. *J. Geophys. Res.*, **101**, 12 331–12 352.

[13] Smagorinsky, J., 1963: General circulation experiments with the primitive equations, I. The basic experiment, *Mon. Wea. Rev.*, **91**, 99–164.

[14] Chu, P.C., M. Huang, and E. Fu, 1996: Formation of the South China Sea warm core eddy in boreal spring. *Proceedings of the Eighth Conference on Air–Sea Interaction*, American Meteorological Society, Boston, 155–159.

[15] Levitus, S. and T. P. Boyer, 1994: World Ocean Atlas 1994: Temperature and Salinity, U.S. Department of Commerce, Washington D.C.

[16] Li Rongfeng, 1991: Simulated results of the current in the South China Sea in summer. in: *Proc. Intern. Symp. Environ. Hydraulics.*, edited by Lee and Cheung, Dec. 16–18, Hong Kong, 957–962.

[17] Li Rongfeng, Wang Wenzhi and Huang Qizhou, 1994: Numerical simulation of the current in the South China Sea in summer, *Chinese Journal of Atmospheric Sciences*, **18**, No.2, 109–114.